Significant Temperature Change and Inhomogeneous Tensile Deformation of Superelastic Ti–26Nb, Ti–25Nb–0.3O and Ti–25Nb–0.3N Shape Memory Alloys



KAROL MAREK GOLASIŃSKI, MICHAŁ MAJ, SANDRA MUSIAŁ, WATARU TASAKI, and HEE YOUNG KIM

In this work, thermomechanical behavior of the superelastic Ti-26Nb, Ti-25Nb-0.3O and Ti-25Nb-0.3N (at. pct) shape memory alloys (SMAs) under load-unload tension was investigated using coupled techniques of infrared thermography and digital image correlation. Local and average characteristics were analyzed in the context of particular deformation stages. In the case of all the SMAs, during loading, first the temperature decreases due to the thermoelastic effect, which can serve to estimate true elastic strain. During further loading, the temperature significantly increases due to the forward stress-induced phase transformation, whereas during unloading, the temperature significantly decreases due to the reverse phase transformation. The average values of the temperature change generated due to the elastocaloric heating and cooling were 15.95 K, 14.94 K, 16.05 K and 17.79 K, 14.44 K, 19.83 K in the case of the Ti-26Nb, Ti-25Nb-0.3O and Ti-25Nb-0.3N SMAs, respectively. The kinematic fields demonstrated that the deformation during loading and unloading is inhomogeneous. It starts with the appearance of thin parallel bands perpendicular to the loading axis. These bands create larger areas with higher strain upon further loading and gradually reappear upon unloading. The results advance the comprehension of the thermal and kinematic aspects of tensile deformation of superelastic Ti-Nb-based SMAs.

https://doi.org/10.1007/s11661-025-08036-4 © The Author(s) 2025

I. INTRODUCTION

THERMOMECHANICAL behavior of materials under tension is directly associated with deformation mechanisms activated during loading. For instance, during purely elastic tension, the temperature signal is linearly decreasing due to the thermoelastic effect. [1,2] Under this assumption, a deviation of the temperature behavior from linearity can serve to indicate the onset of yielding. [3] This strategy has been applied in

experimental studies of various materials, including metals.^[4,5] Analysis of mutual interactions between kinematic and temperature fields is particularly interesting in the case of shape memory alloys (SMAs). This group of materials can exhibit phenomena of shape memory effect or superelasticity due to temperature- or stress-induced martensitic transformation. Nitinol (NiTi), the most widely used SMA, has been comprehensively studied for the last decades. [6-14] Nitinol subjected to tension exhibits an inhomogeneous, Lüders-type deformation accompanied with significant temperature variations. [6-8] The most comprehensive description of the thermomechanical behavior of nitinol was obtained using full-field optical and infrared imagining techniques. Monitoring of the deformation and thermal changes in nitinol associated with the stress-induced phase transformation was presented for the first time in.^[7] Strain fields of nitinol in tension obtained using digital image correlation (DIC) were reported for the first time in.^[9] From then on, full-field quantitative studies regarding propagation and development of stress-induced martensitic bands of nitinol based and other SMAs in tension have been presented in numerous works. Selected results were reviewed in. [15] Temperature

KAROL MAREK GOLASIŃSKI is with the Cardinal Stefan Wyszynski University in Warsaw, Multidisciplinary Research Center, Dewajtis 5, 01-815 Warsaw, Poland Contact e-mail: k.golasinski@uksw.edu.pl. MICHAŁ MAJ and SANDRA MUSIAŁ are with the Institute of Fundamental Technological Research, Polish Academy of Sciences, Pawińskiego 5b, 02-106 Warsaw, Poland. WATARU TASAKI and HEE YOUNG KIM are with the Department of Materials Science, Institute of Pure and Applied Sciences, University of Tsukuba, Tsukuba, Ibaraki 305-8573, Japan. Manuscript submitted March 11, 2025; accepted November 2, 2025.

METALLURGICAL AND MATERIALS TRANSACTIONS A

Published online: 15 November 2025

of the superelastic SMAs during tensile loading significantly increases due to the stress-induced phase transformation, while during unloading it decreases due the reverse transformation. This phenomenon called elastocaloric effect (eCE) has attracted increasing attention as a potential cooling mechanism near room temperature. [16–19] Thus, various SMAs including those based on Co, Fe, Ni and Ti have been studied in order to find the most efficient alloy for elastocaloric cooling applications.^[18,20–22] So far, thermomechanical behavior of a relatively new class of Ni-free Ti-based SMAs under tension has been seldom reported. However, selected Ti-Nb or Ti-Zr-based SMAs have certain properties, which can make them more suitable in the context of solid-state refrigeration. They include among others low driving stress, near-zero hysteresis and relatively good cold workability. [23-26] Few systems have been studied to find high-performance and low-stress SMAs with small hysteresis for elastocaloric cooling. [27-29] Furthermore, thermomechanical behavior of Gum (Ti–23Nb–0.7Ta–2.0Zr–1.2O, at. pct) under tension was analyzed in the context of the nonlinear and superelastic-like deformation. [30–33] The temperature decrease due to elastocaloric cooling was of relatively small around 1.4 K. However, it was shown that the maximum drop of the average temperature of Gum Metal under tension corresponded to the strain value which was significantly lower than the recoverable strain. This a result of the mechanism of nonlinear superelastic-like deformation in Gum Metal due to the high oxygen content 1.2 at. pct and nanometer–sized martensite nanodomains. [34–37] However, by adjusting the chemical composition one can also obtain superelastic Ti-Nb or Ti-Zr SMAs doped with oxygen or nitrogen interstitials, which exhibit a hysteresis loop. [25,36–39] Recently, a full-field kinematic analysis of Ti-25Nb, Ti-25Nb-0.3O and Ti-25Nb-0.7O (at. pct) SMAs under load-unload tension was presented in Reference 40. On the one hand, it was shown that the Ti-25Nb SMA, which exhibits shape memory effect, displays a Lüders-type deformation with pronounced macroscopic bands. On the other hand, it was demonstrated that the local deformation of the superelastic O-added Ti-25Nb SMAs is inhomogeneous but significantly different. In the light of the above, this work concerns a thermomechanical investigation of three superelastic systems Ti-26Nb, Ti-25Nb-0.3O and Ti-25Nb-0.3N (at. pct) with relatively low transformation stress under load-unload tension using full-field imagining techniques. The main objective was to analyze kinematic and thermal characteristics of the SMAs in tension.

II. MATERIALS AND METHODS

The Ti-26Nb, Ti-25Nb-0.3O and Ti-25Nb-0.3N (at.pct) alloys were prepared by the Ar arc melting method using pre-melted sponges of Ti (purity: > 99.7pct) and pure Nb (purity: 99.9pct). The oxygen and nitrogen concentrations of the alloys were adjusted by amount of TiO₂ and TiN powders (purity: 99.9pct), respectively. Homogeneity was ensured by

repeated melting for six times and by flipping of the ingots between the melts. The obtained button-shaped ingots (with diameter of ~ 20 mm, height ~ 10 mm and mass ~ 22 g each) were subsequently sealed in a vacuumed quartz tube and homogenized at 1273 K for 120 min followed by air-cooling. Then the ingots were cold-rolled with a reduction in thickness of 95pct. Specimens were solution-treated at 1173 K for 30 min in an Ar atmosphere, followed by water quenching. In this paper, the as-fabricated state of the SMAs refers to the state after the complete process of fabrication. Specimens for Electron Backscatter Diffraction (EBSD) and X-Ray Diffraction (XRD) measurements and tensile tests were cut using an electro-discharge machine. The damaged surface was removed by chemical etching solution with a composition a $H_2O:HNO_3:HF = 5:4:1$ by volume. EBSD specimens were electropolished at 233 K using a solution of $CH_3OH:C_4H_9OH:HClO_4 = 10:6:1$ by volume. EBSD analyses were performed using a Zeiss Crossbeam 350 Scanning Electron Microscope (SEM) at 500x magnification and 0.5 µm step size. XRD measurements were conducted at room temperature with Cu K_{α} radiation using a Bruker D2 PHASER Benchtop XRD instrument. Displacement-controlled load-unload tensile tests of the SMAs specimens were carried out using an MTS 858 testing machine at room temperature. Maximal displacement of 0.35 mm and displacement rate of 0.12 mm·s⁻¹ were used. A technical drawing of the tested specimens is shown in Figure 1(a). The gauge part of each specimen was 4 mm \times 6 mm \times 0.5 mm. Taking into account the specimen's geometry, a maximum strain of around 2 pct and an average strain rate of 2 · 10 (relatively close to adiabatic conditions) were applied. This class of Ti-Nb SMAs exhibits recovery strain of around 2 pct upon unloading. [23–26] Thus, the maximum strain under load was selected to analyze the themomechanical behavior of the SMAs during the superelastic deformation, which is also interesting in the view of elastocaloric effect. One surface of the specimen was covered with soot in order to increase and make uniform the emissivity of the specimen's surface for temperature determination on the basis of infrared radiation measurements (assumed emissivity of soot layer: 0.95). The other surface of the specimen was also covered with soot but additionally a small dots of white paint were sprayed onto the soot layer to obtain an adequate pattern for digital image correlation (DIC) algorithm. A region of interest (ROI), which was used for further full-field thermomechanical analysis, is marked in the gauge part of the specimen, as presented in Figure 1(b). The deformation process of each specimen was simultaneously monitored by a visible range (0.4 µm-1 µm) sCMOS PCO Edge 5.5 camera and an infrared range (3 μ m–5 μ m) ThermaCam Phoenix camera. The loading force as a function of time and two image sequences in the visible and infrared ranges were recorded. The settings of the sCMOS PCO Edge 5.5 camera were the following: the image size 931 pixels × 1280 pixels what gave pixel size equal to 7.7 μ m, the recording frequency of the camera was equal to 100 Hz.

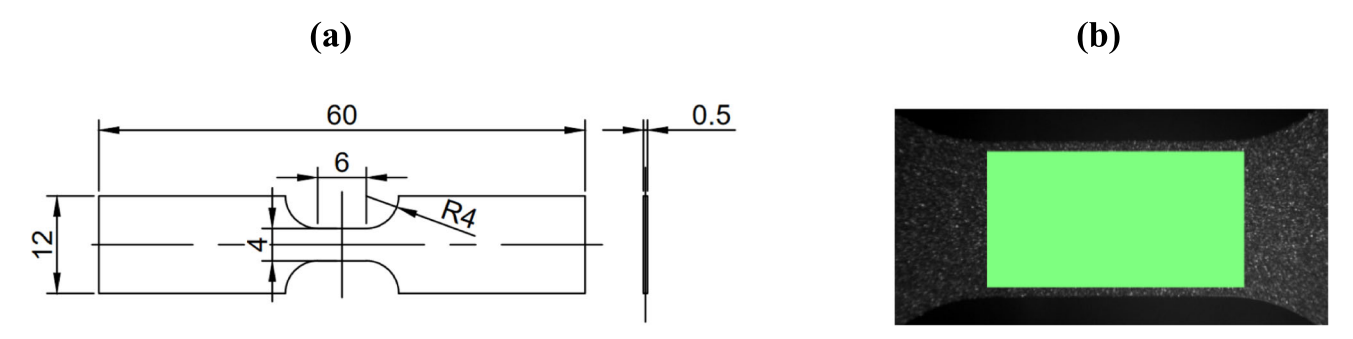


Fig. 1—(a) a technical drawing of the tested specimens and (b) a ROI marked in the gauge part.

Hencky strain ε_{yy} and strain rate $\dot{\varepsilon}_{yy}$ fields (where y is the loading direction) were determined on the basis of the displacement fields measured using a 2D DIC method implemented in a ThermoCorr software. [41] In particular, the mean Hencky strain $\overline{\epsilon}_{yy}$ was calculated on the basis of displacement fields obtained by DIC using so called 'virtual extensometers' of the initial length of 6 mm placed in the gauge part of each specimen. The temperature field during the deformation of the SMAs specimen was obtained based on the IR radiation emitted from the specimen's surface and registered by a ThermaCam Phoenix IR camera with high thermal sensitivity up to 0.02 K and at the recording frequency 200 Hz. The mean temperature was determined based on the obtained temperature distribution from the ROI of the specimen.

The temperature change ΔT is expressed by Eq. [1]:

$$\Delta T = T(t) - T(t_0) \tag{1}$$

where T(t) is the mean value of the temperature calculated for the ROI of the tested specimen at each instant of straining and $T(t_0)$ is the mean temperature of the ROI before the deformation. The mean temperature of all material points in the defined region can be calculated at each instant of straining. The Thermocorr software, used in this research, enabled to apply the coupling procedure of the experimental results when the DIC and IRT were simultaneously used. Exemplary applications of the ThermoCorr software for characterization of various materials including Gum Metal, aluminum multicrystal and stainless steel are described in. $^{[42-44]}$ The detailed numerical procedures are presented in. $^{[45]}$

III. EXPERIMENTAL RESULTS

A. Phase Contents and Microstructure of As-Fabricated SMAs

XRD profiles of as-fabricated Ti–26Nb, Ti–25Nb–0.3O and Ti–25Nb–0.3N SMAs determined for $69^{\circ} < 2\theta < 72^{\circ}$ are shown in Figure 2. In the initial state the peaks corresponding only to β phase were identified.

Orientation maps of as-fabricated Ti–26Nb, Ti–25Nb–0.3O, and Ti–25Nb–0.3N SMAs with respect to the normal direction (ND) [001] and rolling direction (RD) [010] are presented in Figures 3(a) and (b), respectively.

The inverse pole figure (IPF) maps show that the alloys are composed of body-centered cubic (bcc) β phase grains. Furthermore, all SMAs reveal a comparable crystallographic texture characterized primarily by the $\langle 011 \rangle \parallel$ RD fiber. Within this fiber, the $\{211\}\langle 110 \rangle$ orientation component is particularly pronounced in the Ti–25Nb–0.3N SMA.

B. Global Thermomechanical Characteristics of the SMAs Under Load-Unload Tension

Force vs. displacement and true stress vs. true strain curves of Ti–26Nb, Ti–25Nb–0.3O and Ti–25Nb–0.3N SMAs under load-unload tension are shown in Figures 4(a) and (b), respectively. Curves of all the SMAs investigated in this work show superelastic hysteresis loops. Temperature change vs. time curves of the SMAs are presented in Figure 4(c).

During tensile loading of all SMAs considered in this work, first the temperature decreases due to the thermoelastic effect. This can serve to estimate the range of the true elastic deformation corresponding to the transformation strain of SMAs. Minimum temperature ΔT_{min} and the corresponding values of the stress $\sigma_{\Delta T_{min}}$ and the strain $\overline{\epsilon}_{\Delta T}$, are given in Table I.

and the strain $\overline{\epsilon}_{\Delta T_{\rm min}}$ are given in Table I. In the case of Ti–26Nb, the values $\sigma_{\Delta T_{\rm min}}=61$ MPa and $\overline{\epsilon}_{\Delta T_{\rm min}}=0.09$ are lower when compared to the SMAs doped with interstitial atoms. The Ti–25Nb–0.3O SMA exhibits the largest values $\sigma_{\Delta T_{\rm min}}=212$ MPa and $\overline{\epsilon}_{\Delta T_{\rm min}}=0.37$, whereas the values of the Ti–25Nb–0.3N SMA are $\sigma_{\Delta T_{\rm min}}=140$ MPa and $\overline{\epsilon}_{\Delta T_{\rm min}}=0.27$. This indicates that the addition of oxygen and nitrogen interstitials elevates, to varying degrees, the critical stress necessary to induce the martensitic transformation. This phenomenon is evidenced by recorded temperature decreases associated with the thermoelastic effect.

Further loading of the SMAs generates heating associated with the exothermic stress-induced phase transformation. During unloading, the temperature decreases due to the elastocaloric cooling. The mean values of the temperature growth $\Delta T_{\rm eH}$ and decrease

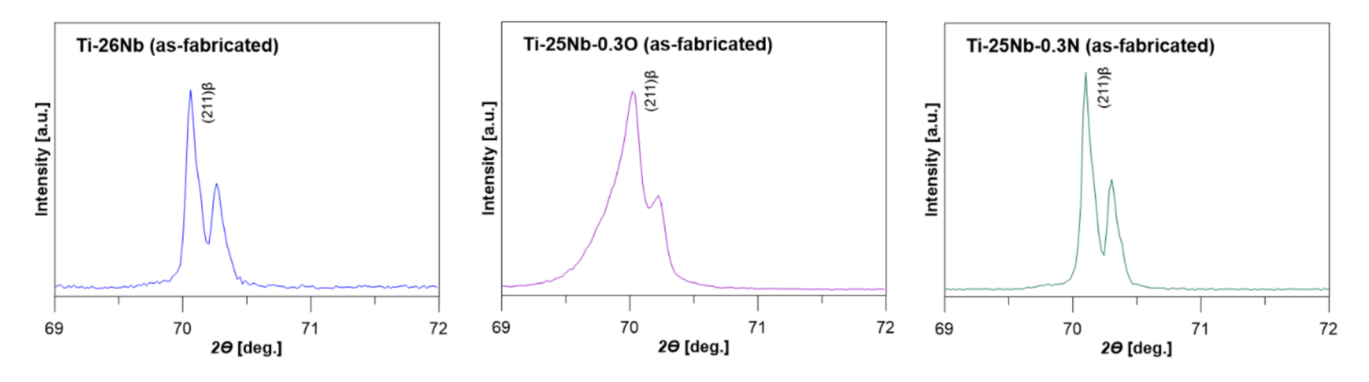


Fig. 2—XRD profiles of as-fabricated Ti-26Nb, Ti-25Nb-0.3O and Ti-25Nb-0.3N SMAs.

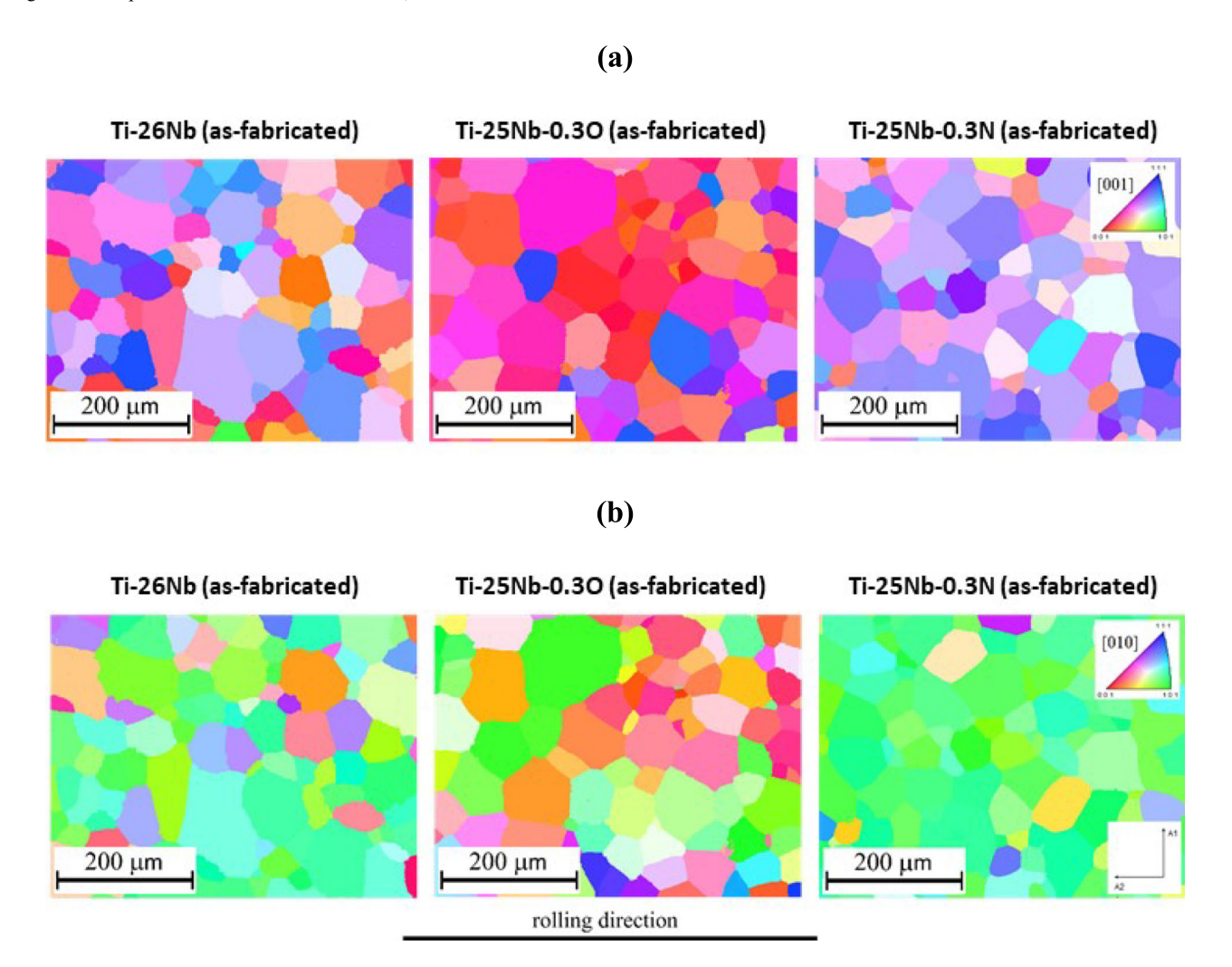


Fig. 3—Orientation maps of as-fabricated Ti-26Nb, Ti-25Nb-0.3O and Ti-25Nb-0.3N SMAs with respect to: (a) ND ([001]) and (b) RD ([010]).

 $\Delta T_{\rm eC}$ and the recoverable strain $\overline{\epsilon}_{\rm r}$ are given in Table II. The values of the $\Delta T_{\rm eH}$ are 15.95 K, 14.94 K and 16.05 K, whereas those of the temperature drop $\Delta T_{\rm eC}$ are 17.79 K, 14.44 K and 19.83 K for Ti–26Nb, Ti–25Nb–0.3O and Ti–25Nb–0.3N, respectively. The values of the recoverable strain $\overline{\epsilon}_{\rm r}$ are 1.56, 1.81 and 1.94 for Ti–26Nb, Ti–25Nb–0.3O and Ti–25Nb–0.3N, respectively.

C. Full-Field thermomechanical Characterization of the SMAs Under Load-Unload Tension

Full-field thermomechanical characteristics of the Ti–26Nb, Ti–25Nb–0.3O and Ti–25Nb–0.3N SMAs under load-unload tension are shown in Figures 5(a through c), respectively. Strain, strain rate (A)–(H) and temperature fields (A*)–(H*) were captured at selected

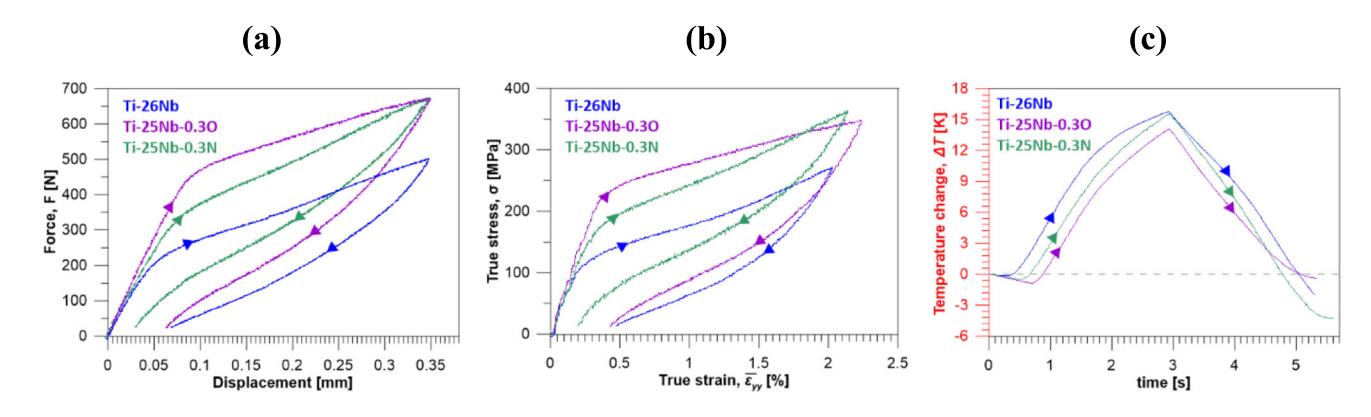


Fig. 4—(a) Force vs. displacement, (b) true stress vs. true strain curves and (c) temperature change vs. time curves of Ti–26Nb, Ti–25Nb–0.3O and Ti–25Nb–0.3N SMAs under load-unload tension.

Table I. Minimum Temperature ΔT_{\min} and the Corresponding Values of Stress $\sigma_{\Delta T_{\min}}$ and Strain $\overline{\epsilon}_{\Delta T_{\min}}$ of Ti–26Nb, Ti–25Nb–0.3O and Ti–25Nb–0.3N SMAs

Composition [at. pct]	$\Delta T_{\min}[K]$	$\sigma_{\Delta T_{ m min}}[{ m MPa}]$	$\overline{\varepsilon}_{\Delta T_{\min}}[\mathrm{pct}]$
Ti-26Nb Ti-25Nb-0.3O	- 0.16 - 0.86	61 212	0.09
Ti-25Nb-0.3N	- 0.49	140	0.27

Table II. Temperature Growth $\Delta T_{\rm eH}$, Temperature drop $\Delta T_{\rm eC}$ and Recoverable Strain $\overline{\rm e}_{\rm r}$ of Ti-26Nb, Ti-25Nb-0.3O and Ti-25Nb-0.3N SMAs

	Temperature increase [K]	Temperature decrease [K]	Recoverable strain [pct]
Composition [at.pct]	$\Delta T_{ m eH}$	$\Delta T_{ m eC}$	$\overline{\epsilon}_{r}$
Ti-26Nb Ti-25Nb-0.3O Ti-25Nb-0.3N	15.95 14.94 16.05	17.79 14.44 19.83	1.56 1.81 1.94

instants of loading and unloading corresponding to the following values of $\overline{\epsilon}_{vv}$

- (A) $\overline{\epsilon}_{yy} = 0.3 \text{pct (during loading)}$
- (B) $\overline{\epsilon}_{yy} = 0.5 \text{pct (during loading)}$
- (C) $\overline{\epsilon}_{yy} = 1.0 \text{pct (during loading)}$
- (D) $\overline{\epsilon}_{yy} = 1.5 \text{pct (during loading)}$
- (E) $\overline{\varepsilon}_{yy} = \overline{\varepsilon}_{max}$ (maximal strain during loading)
- (F) $\overline{\varepsilon}_{yy} = 1.5pct(during unloading)$
- (G) $\overline{\epsilon}_{yy} = 1.0pct(during unloading)$
- (H) $\overline{\epsilon}_{yy} = \overline{\epsilon}_{un}(after unloading)$

Both kinematic and temperature fields clearly indicate that the deformation of Ti–26Nb, Ti–25Nb–0.3O and Ti–25Nb–0.3N SMAs is inhomogeneous from the beginning of loading process. However the strain ε_{yy} and strain rate $\dot{\varepsilon}_{yy}$ fields give more accurate deformation patterns, whereas the temperature fields are blurred. The full–field thermomechanical characteristics presented in Figures 6(a through c) prove that the deformation

proceeds in a similar manner for each SMA. Narrow, pararell bands perpendicular to the loading axis apear in kinematic fields determined at (A). A number of deformation bands increase with the deformation process (B)–(C). Then, the bands gradually merge and form larger areas with higher strain at the final stage of loading (D)-(E). During unloading, shape recovery proceeds in an inhomogeneous manner (F)-(G)-(H). However, distinct differences are observed in the strain fields of Ti-25Nb-0.3O and Ti-25Nb-0.3N. In the case of Ti-25Nb-0.3O, the strain field in the upper part of the sample appears to be frozen, with no visible changes during unloading. This suggests that the reverse transformation is highly inhomogeneous and that certain regions of the sample do not complete the transformation. In contrast, for Ti-25Nb-0.3N, the strain maps in the final stage of unloading (G)-(H) indicate almost complete shape recovery. Several deformation bands can be still observed in kinematic fields captured just after unloading at stage (H).

Additionally, shape recovery due to the reverse martensitic transformation upon heating after unloading was evaluated for all the studied SMAs. The shape memory effect was observed in the Ti–26Nb and Ti–25Nb–0.3O alloys, whereas the Ti–25Nb–0.3N alloy exhibited superelastic behavior with no shape recovery upon heating.

The instantaneous changes in the local values of $\dot{\epsilon}_{yy}$ are macroscopic manifestations of the phase transformation kinetics occurring at the microscopic scale in Ti–26Nb, Ti–25Nb–0.3O and Ti–25Nb–0.3N SMAs under load–unload tension, as shown in the spatiotemporal graphs of $\dot{\epsilon}_{yy}$ presented in Figures 6(a through c), respectively.

The spatiotemporal graphs illustrate the relationship between the variation in the local $\dot{\epsilon}_{yy}$ along the vertical axis of symmetry of the sample and the time during the deformation process. Accordingly, the graphs show the y-coordinates of the points located along the vertical axis of symmetry of the sample at successive moments of tension. The spatiotemporal plots were obtained based on the profiles marked on the strain rate $\dot{\epsilon}_{yy}$ fields on the sample's surface in the reference configuration. Comparing the spatiotemporal graphs for the studied alloys,

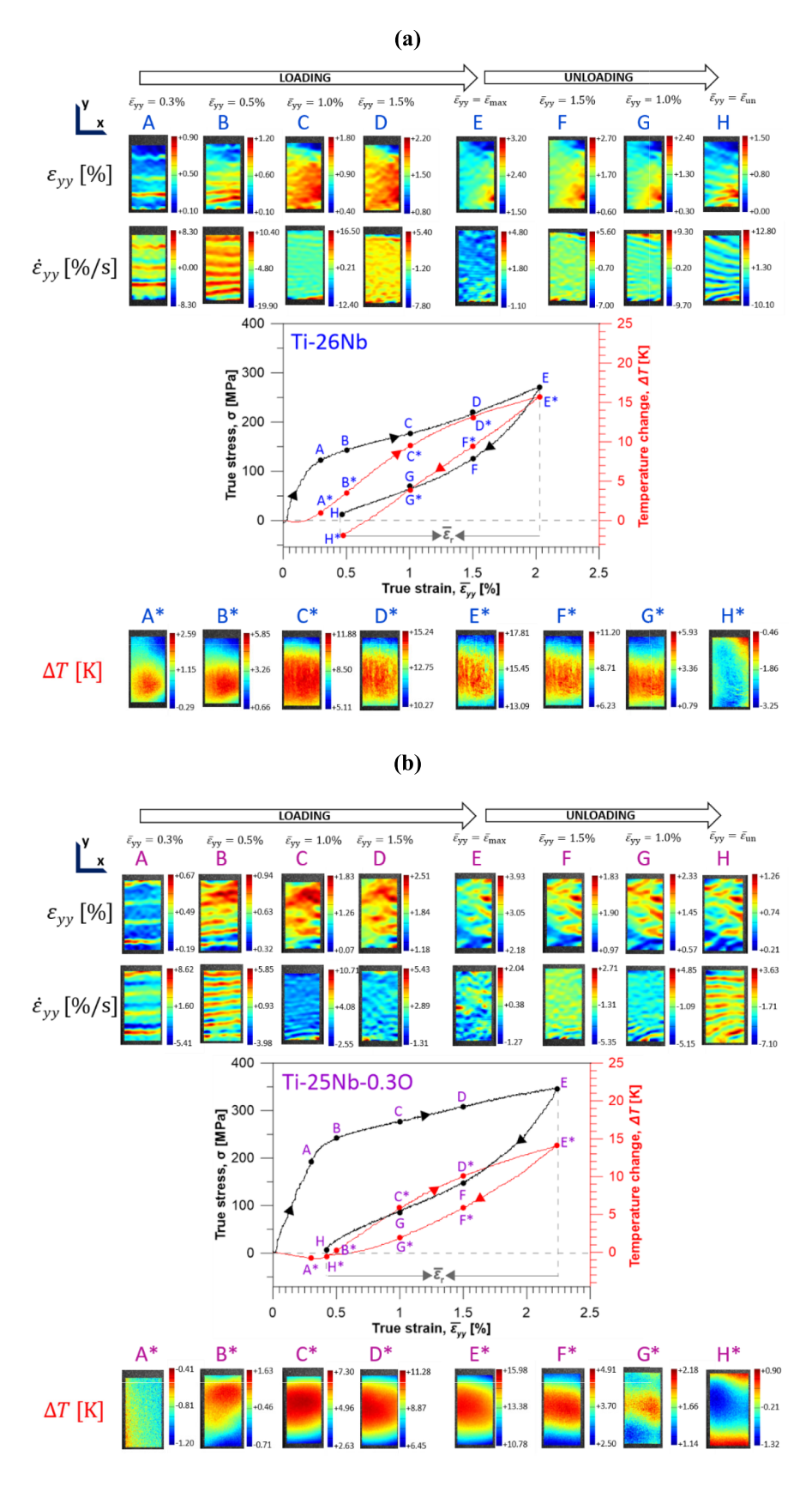


Fig. 5—Strain ε_{yy} , strain rate $\dot{\varepsilon}_{yy}$ and temperature ΔT fields of (a) Ti–26Nb, (b) Ti–25Nb–0.3O and (c) Ti–25Nb–0.3N SMAs under load–unload tension at selected stages of deformation.

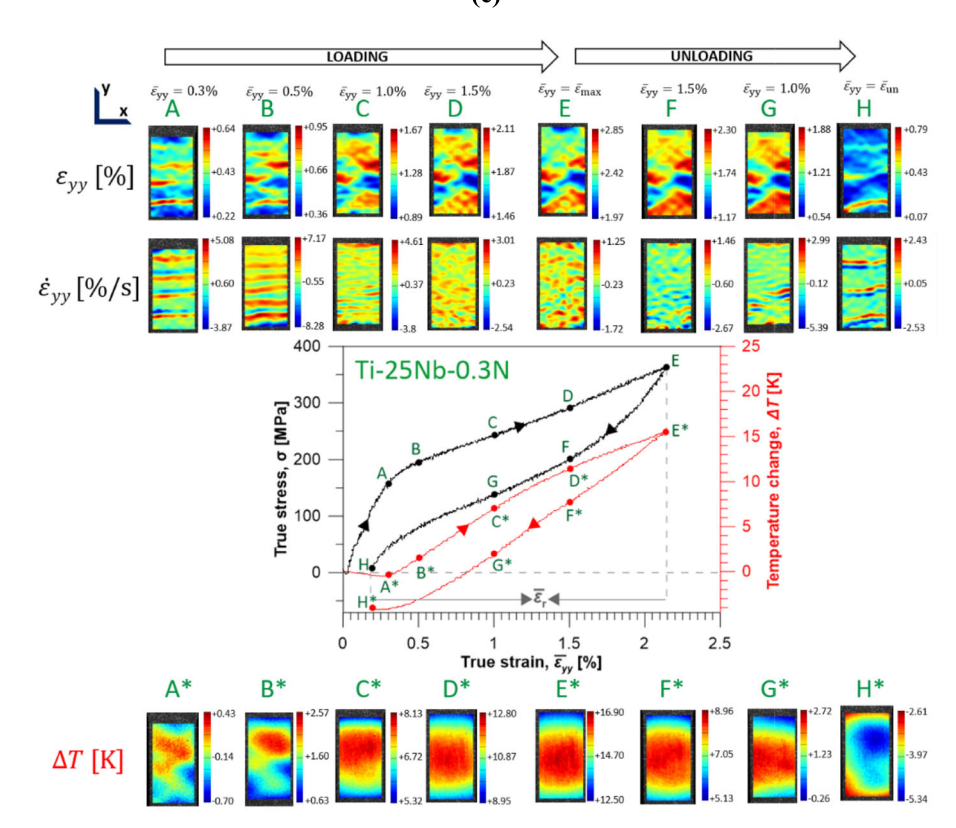


Fig. 5—continued.

it can be observed that the loading behavior is quite similar across all of them. However, during unloading, the bands in Ti–25Nb–0.3O are the least intense and appear only in the lower part of the gauge section. This may indicate that the reverse transformation is the most inhomogeneous in this alloy, and that in certain regions of the sample, the reverse transformation may not be fully completed. Maximum local values of strain ε_{yy} , strain rate $\dot{\varepsilon}_{yy}$ and temperature ΔT of Ti–26Nb, Ti–25Nb–0.3O and Ti–25Nb–0.3N SMAs under load–unload tension are listed in Table III.

Maximum local values of strain rate $\dot{\epsilon}_{yy_max}$ of the SMAs considered in this work were over five times higher than those of global strain rate at particular stages of tension. Maximum local values of temperature ΔT_{max} were around 2 K higher than the mean values of the temperature increase ΔT_{eH} values listed in Table I.

D. Phase Contents and Microstructure of the SMAs After Unloading

XRD profiles of Ti–26Nb, Ti–25Nb–0.3O, and Ti–25Nb–0.3N SMAs after unloading, recorded in the range $69^{\circ} < 2\theta < 72^{\circ}$, are presented in Figure 7. The orthorhombic α'' martensite was identified in all SMAs after unloading, with the lowest fraction detected in the Ti–25Nb–0.3N alloy.

Crystallographic orientation maps of deformed and unloaded Ti-26Nb, Ti-25Nb-0.3O, and Ti-25Nb-0.3N SMAs with respect to the ND and RD are shown in Figures 8(a) and (b), respectively. The tensile axis was aligned with the RD, and the $\langle 011 \rangle \parallel$ RD fiber seems to be more pronounced in the unloaded state than in the initial state. Deformation twins are observed only in the Ti-25Nb-0.3O SMA, specifically in grains belonging to the $\langle 011 \rangle \parallel$ RD fiber. However, in some cases, they are close to the resolution limit of the analysis. This crystallographic orientation facilitates twin propagation across several grains with only minor directional deviations, rather than their arrest at grain boundaries. The deformation twins present in the unloaded state account for the irreversible strain in the oxygen-doped SMA. A high-magnification map (acquired with a scanning step of 30 nm) and the corresponding misorientation profiles, presented in Figures 9(a through c), provide a more detailed characterization of deformation twinning in the Ti–25Nb–0.3O alloy.

In addition to the primary twins typical of the bcc structure, secondary twins are also observed. The results obtained may indicate the presence of the α'' phase, particularly at the twin–matrix interface; however, the spatial resolution of the EBSD measurements is insufficient to draw a definitive conclusion.

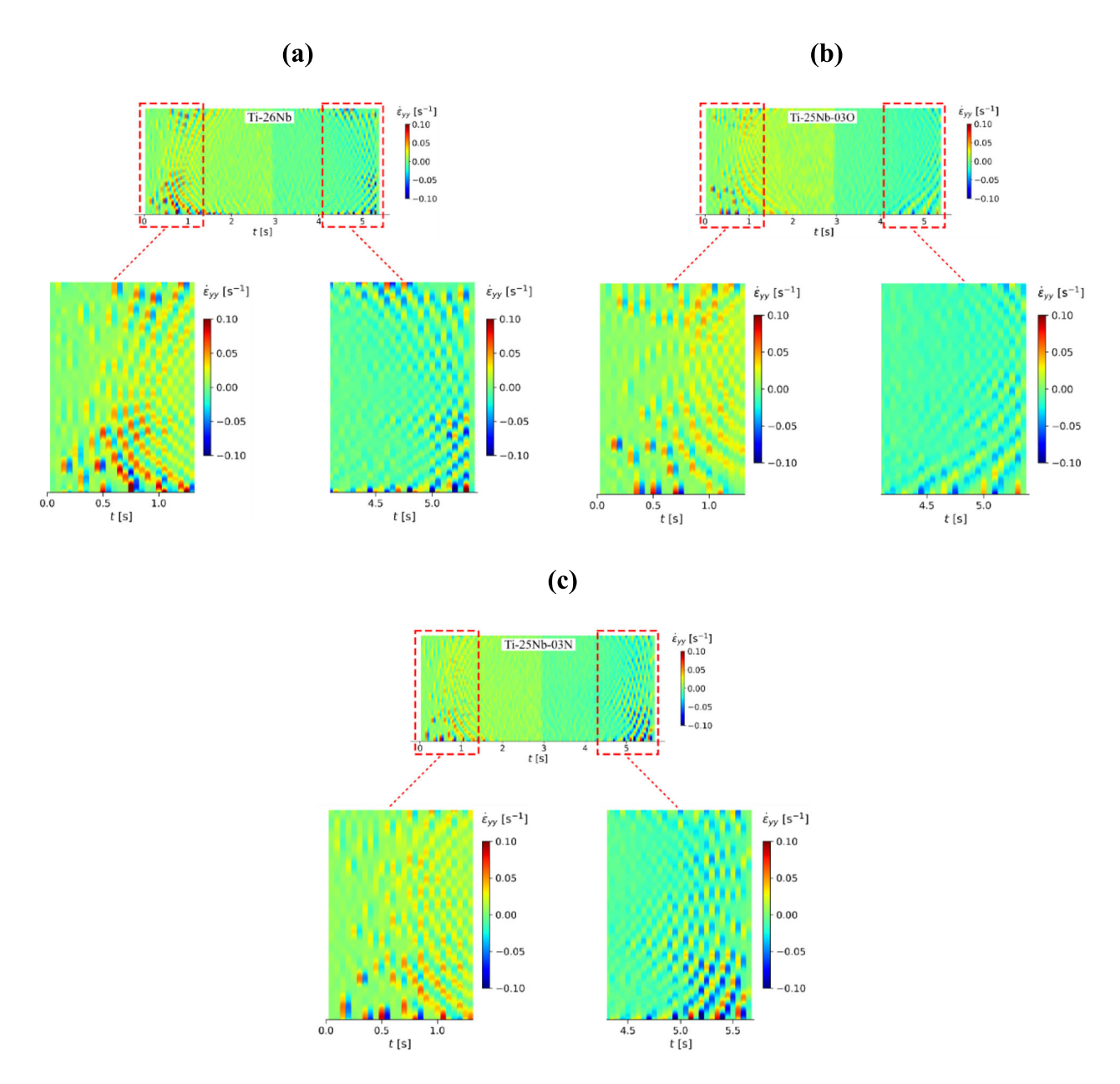


Fig. 6—Spatiotemporal graphs of strain rate $\dot{\epsilon}_{yy}$ of (a) Ti-26Nb, (b) Ti-25Nb-0.3O and (c) Ti-25Nb-0.3N SMAs under load-unload tension.

IV. DISCUSSION

Superelasticity and shape memory effect in Ti–Nb-based SMAs is associated with the stress or temperature induced martensitic phase transformation from the bcc β phase to the orthorhombic α'' martensite. Both shuffle and shear are involved in this deformation mechanism. Stress-induced α'' martensite was identified in the in situ microscopic observations and XRD patterns captured during the superelastic deformation of Ti–26Nb SMA in tension. All SMAs studied in this work, in the as-fabricated state, consist of bcc β -phase grains. Notably, the Ti–25Nb–0.3N alloy exhibits a relatively strong $\{112\}\langle110\rangle$ recrystallization texture. This can be attributed to the dual effect of nitrogen: it increases the stored energy during deformation, promoting the nucleation of recrystallization, while

simultaneously inhibiting excessive grain growth through grain boundary pinning, thereby stabilizing the recrystallization texture. Orthorhombic α'' martensite was identified using XRD analysis in all the SMAs after unloading, with the Ti-25Nb-0.3N alloy exhibiting the lowest amount of this phase. Deformation twins are found exclusively in the Ti-25Nb-0.3O SMA, occurring in grains belonging to the (011) RD fiber. Moreover, the results suggest a possible presence of the α'' phase, especially at the twin-matrix interface; however, the spatial resolution of performed EBSD measurements does not allow a definitive conclusion. However, the addition of interstitial atoms changes the stress-strain behavior of the Ti-Nb SMAs. [25,34-39] For all the SMAs considered in this work, the macroscopic deformation develops in a form of narrow parallel bands, which

Table III. Maximum Local Values of Strain ε_{yy} Strain Rate $\dot{\varepsilon}_{yy}$ and Temperature ΔT of Ti–25Nb–0.3O and Ti–25Nb–0.3N SMAs Under Load–Unload Tension

	Maximum Strain [pct]	Maximum Strain Rate [pct \bullet s^{-1}]	Maximum Temperature [K]
Composition [at. pct]	$\varepsilon_{ m yy_max}$	$\dot{arepsilon}_{ m yy_max}$	$\Delta T_{ m max}$
Ti-26Nb Ti-25Nb-0.3O Ti-25Nb-0.3N	3.1 3.9 2.9	11.1 10.7 16.0	17.32 15.98 16.95

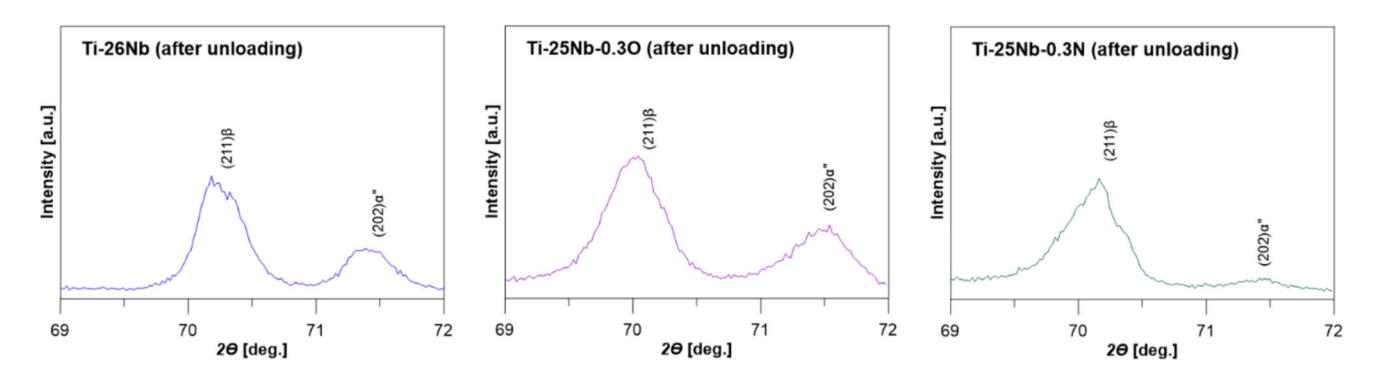


Fig. 7—XRD profiles of Ti-26Nb, Ti-25Nb-0.3O and Ti-25Nb-0.3N SMAs after unloading.

create larger zones with higher values of strain upon further loading due to the forward stress-induced phase transformation. These zones gradually disappear due to the reverse phase transformation and the parallel bands reappear upon unloading. In, [40] it was shown this type of the O-added Ti-25Nb SMAs exhibit a similar type of deformation. This work proves that other superelastic systems, namely Ti-26Nb and Ti-25Nb-0.3N, present this peculiar kind of deformation under tension. To note, in the case of the SMAs, which exhibit a Lüders-type deformation, e.g.: Ni-Ti or Ti-25Nb, the angle of inclination of kinetic band measured with respect to the loading direction is up to 55°. [6-15,40] The potential reason can be associated with the critical composition of the SMAs and the change of the underlying deformation mechanism of superelasticity, however this hypothesis needs further detailed investigations. In this study, the narrowest hysteresis and the most intensive reverse transformation during unloading was observed for the Ti-25Nb-0.3N alloy. The stressstrain curve of this SMA exhibits the highest value of reversible strain $\overline{\epsilon}_r$ which was confirmed by the XRD profile after unloading showing the smallest fraction of the α'' martensite among all the SMAs. Thus, the addition of nitrogen results in better superelastic behavior for the given Ti-Nb SMA composition compared to the addition of oxygen. On the other hand, for the Ti-25Nb-0.3O alloy exhibited the highest increase in the critical stress for slip and for inducing martensite, while still maintaining a significant superelastic recovery. The results of our work show that the temperature increase $\Delta T_{\rm eH}$ and decrease $\Delta T_{\rm eC}$ generated during tensile unloading of the SMAs exceeded 14 K in a single load-unload tension cycle, as presented in Table II.

They are lower than those of Nitinol, which are greater than 30 K during a single load-unload tension cycle, as reported in.[10,11] On the one hand, a relatively low transformation stress of Ti-26Nb, Ti-25Nb-0.3O and Ti-25Nb-0.3N SMAs (under 213 MPa), which was their drawback for biomedical applications, can be beneficial in the area of elastocaloric devices. It is significantly lower when compared to that of Nitinol (usually over 550 MPa). Additionally, this class of alloys have good cold workability, which can be advantageous in the view of the complicated manufacture technology of Nitinol. On the other hand, the Ti-Nb SMAs suffer from instable superelastic deformation. [32-34] Their superelasticity is not fully recoverable and they significantly change stress-strain response under cyclic tension. It was shown that with an increasing number of cycles, the transformation stress and superelastic strain decreased, while the stress hysteresis became narrow. An attempt to improve the stability of the superelastic behavior of Ti-26Nb SMA during cyclic tension by selected thermomechanical treatments for microstructure control such as low temperature annealing and aging was presented in. [24] Most stabilized superelasticity of Ti-26Nb SMA was ascribed to the combined effect of work hardening and fine isothermal ω -phase precipitation. However, it was insufficient for potential elastocaloric applications. The addition of interstitial alloying elements was another strategy for improving cyclic stability of superelastic properties due to the increase in the critical stress for slip by the solid solution strengthening effect. Specifically, in the case of the Ti-23Nb-1.0N SMA stable cyclic deformation behavior was observed when compared with the Ti-26Nb SMA. Around 2.2pct of superelastic strain was obtained even

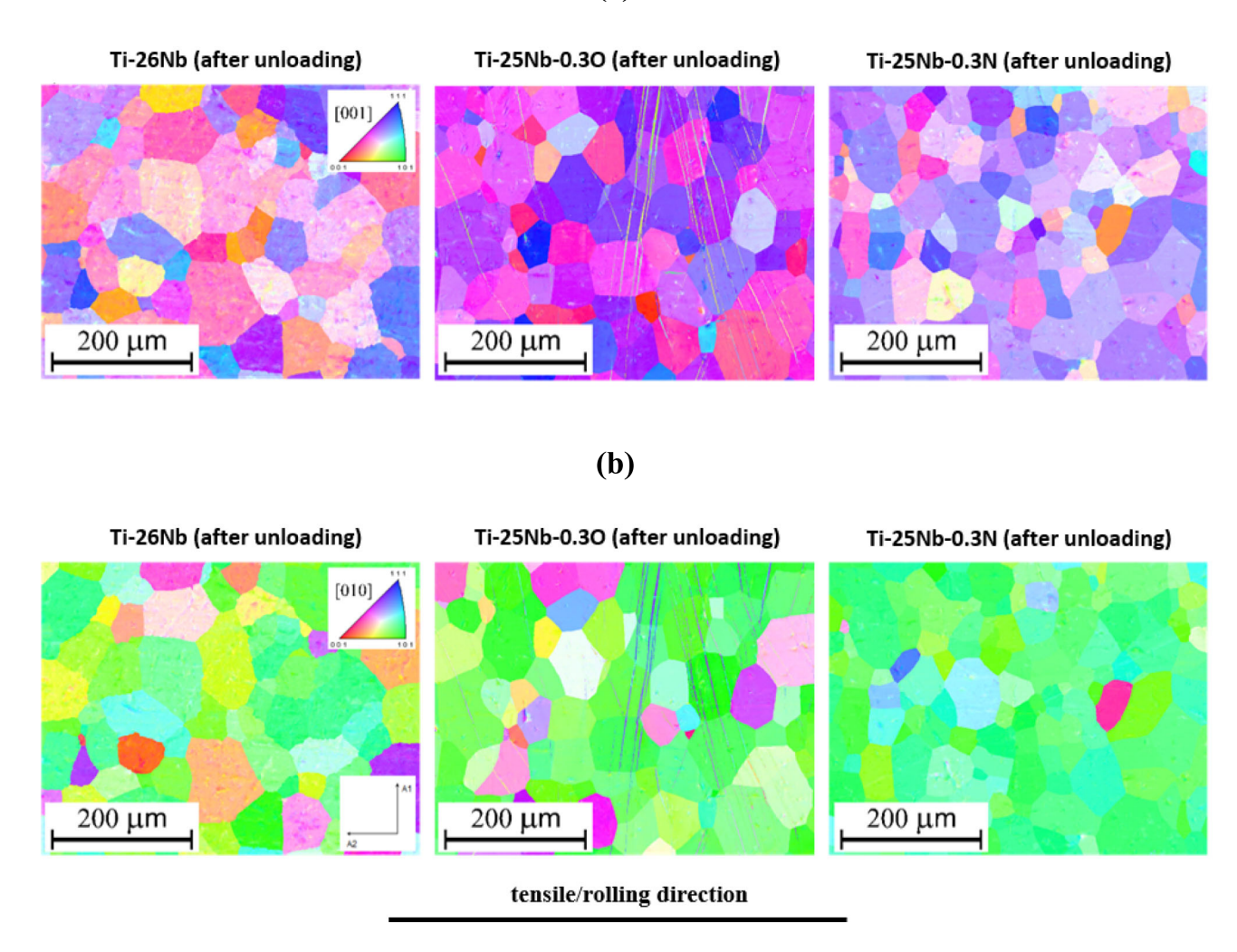


Fig. 8—EBSD maps of Ti-26Nb, Ti-25Nb-0.3O, and Ti-25Nb-0.3N SMAs after unloading with respect to: (a) ND ([001]) and (b) RD ([010]).

at the 500th cycle. Thus, this SMA can be a more suitable candidate for elastocaloric applications. Recently, selected Ti–Zr and Ti–Nb-based SMAs systems, with the adiabatic temperature change measured during unloading between

2.5 K and 8 K, were studied in. [27–29] Homogeneous deformation combined with small hysteresis, which are important features in the context of cyclic stability, were achieved. Major challenges considering the development of solid–state refrigerants include achieving high performance combined with good structural and functional properties as well as low processing cost. [46] Further investigations of the β –Ti superelastic alloys aimed at overcoming their intrinsic problems with the use of full–field thermomechanical characterization can contribute to potential applications in the area of solid state heating and cooling systems.

V. CONCLUDING REMARKS

The thermomechanical behavior of the Ti–26Nb, Ti–25Nb–0.3O and Ti–25Nb–0.3N SMAs under load–unload tension was studied using synchronized techniques of IRT and DIC. The results provide insight into the thermal and kinematic aspects of the deformation of the SMAs at the macroscopic scale. The following conclusions can be drawn:

- (1) The average temperature change can serve to estimate specific deformation stages of the Ti–26Nb, Ti–25Nb–0.3O and Ti–25Nb–0.3N SMAs, including true elasticity accompanied by a temperature decrease, as well as superelasticity with exothermic loading and endothermic unloading.
- (2) The deformation of the Ti-26Nb, Ti-25Nb-0.3O, and Ti-25Nb-0.3N SMAs under tension was

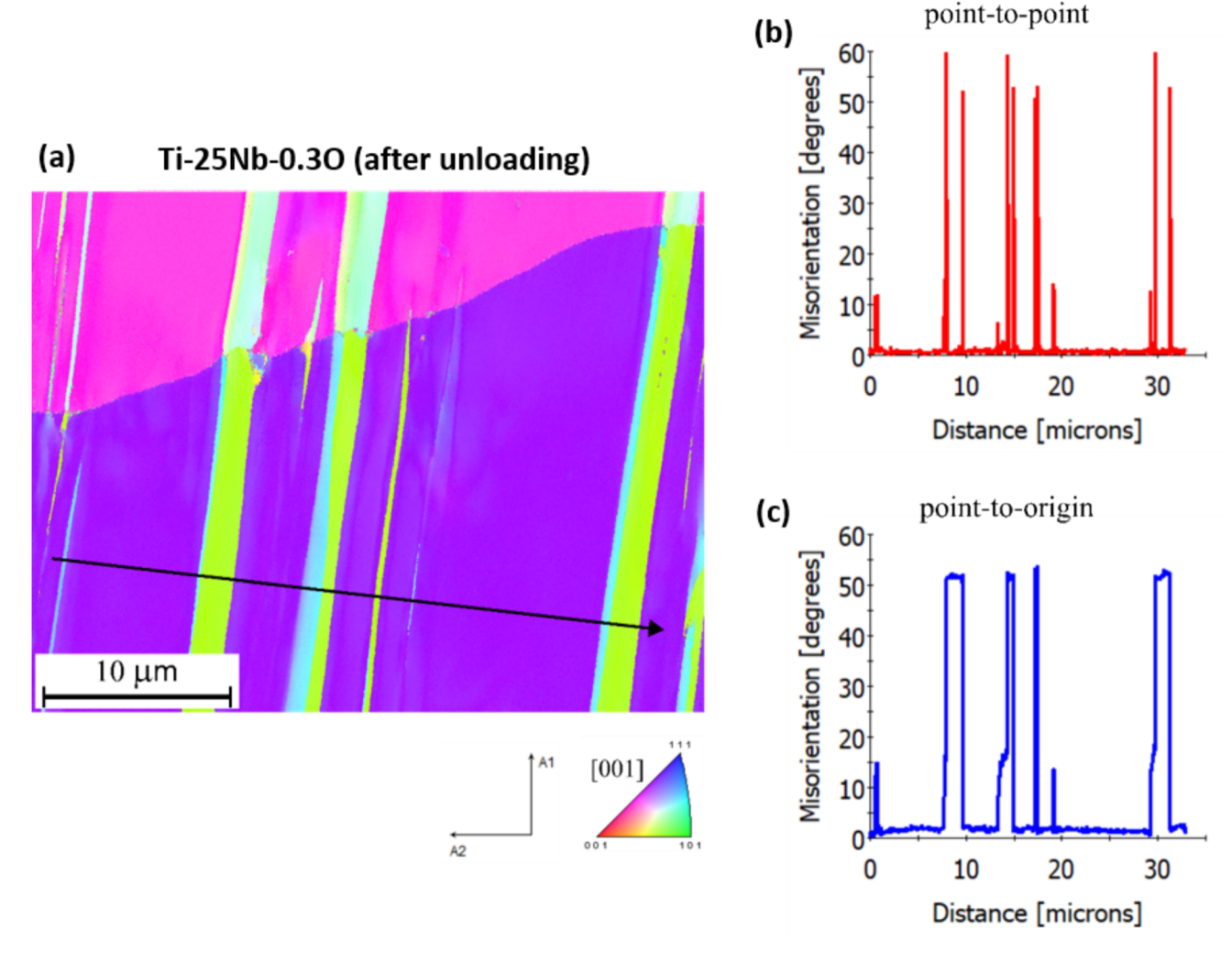


Fig. 9—(a) High magnification EBSD map of Ti-25Nb-0.3O after unloading and (b) point-to-point and (c) point-to-origin misorientation profiles along black arrow marked on the EBSD map.

found to be inhomogeneous from the beginning of the loading process as demonstrated in ε_{yy} , $\dot{\varepsilon}_{yy}$ and ΔT fields. The kinematic fields gave a better description of the inhomogeneity of the SMAs under tension. It was shown that at the beginning of the loading process, the SMAs exhibit narrow, parallel bands perpendicular to the loading axis. Subsequent loading generates an increasing number of bands appearing in the SMAs, which further merge and form inhomogeneous areas of deformation.

- (3) The temperature increase generated during loading and the temperature increase generated during unloading in all the SMAs considered in this work exceeded 14 K. The Ti–25Nb–0.3N SMA demonstrated the highest temperature change, the highest recoverable strain and a relatively low critical transformation stress.
- (4) The addition of nitrogen enhances the superelastic behavior of the given Ti–Nb SMA composition more effectively than oxygen. In contrast, the Ti–25Nb–0.3O alloy shows the greatest increase in the critical stress for slip and for inducing martensite, while still exhibiting a noticeable superelastic recovery.
- (5) Certain drawbacks of the Ti–26Nb, Ti–25Nb–0.3O and Ti–25Nb–0.3N SMAs, such as insufficient superelastic stability and inhomogeneous deformation, do not make them good candidates for elastocaloric heating or cooling applications. However, it is confidently believed that the β –Ti superelastic alloys with improved properties will play a role in this field.

ACKNOWLEDGMENTS

Karol M. Golasiński acknowledges the support of the Japan Society for the Promotion of Science (JSPS) Postdoctoral Fellowship (ID No. P20812). The research was funded by the National Science Center, Poland through the Grant 2023/48/C/ST8/00038. The authors would like to express their gratitude to Leszek Urbański from IPPT PAN for conducting tensile tests and processing the related data.

DATA AVAILABILITY

The data supporting the findings of this study are openly available in Zenodo at https://doi.org/10.5281/z enodo.17350580.

COMPETING INTERESTS

The authors declare that they have no known competing financial interests or personal relationships that could have appeared to influence the work reported in this paper.

OPEN ACCESS

This article is licensed under a Creative Commons Attribution 4.0 International License, which permits use, sharing, adaptation, distribution and reproduction in any medium or format, as long as you give appropriate credit to the original author(s) and the source, provide a link to the Creative Commons licence, and indicate if changes were made. The images or other third party material in this article are included in the article's Creative Commons licence, unless indicated otherwise in a credit line to the material. If material is not included in the article's Creative Commons licence and your intended use is not permitted by statutory regulation or exceeds the permitted use, you will need to obtain permission directly from the copyright holder. To view a copy of this licence, visit http://creat ivecommons.org/licenses/by/4.0/.

REFERENCES

- 1. W. Thomson: Trans. R. Soc. Edinb., 1853, vol. 20(2), pp. 261-8.
- J.P. Joule and W. Thomson: Dublin Philosophical Magazine J. Sci., 1852, vol. 28, pp. 481–92. https://doi.org/10.1080/ 14786445208647169.
- 3. B.A. Boley and J.H. Weiner: *Theory of thermal stresses*, Dover Publications, Newburyport, 2012.
- W. Oliferuk, M. Maj, R. Litwinko, and L. Urbański: Eur. J. Mech. A. Solids, 2012, vol. 35, pp. 111–8. https://doi.org/10.1016/j.euromechsol.2011.08.007.
- S. Vitzthum, J.R. Kornmeier, M. Hofmann, M. Gruber, E. Maawad, A.C. Batista, C. Hartmann, and W. Volk: *Mater. Des.*, 2022, vol. 219, p. 110753. https://doi.org/10.1016/j.matdes.2022. 110753
- S. Miyazaki, T. Imai, K. Otsuka, and Y. Suzuki: Scr. Mater., 1981, vol. 15(8), pp. 853–6. https://doi.org/10.1016/0036-9748(81) 90265-9

- J.A. Shaw and S. Kyriakides: J. Mech. Phys. Solids, 1995, vol. 43(8), pp. 1243–81. https://doi.org/10.1016/0022-5096(95)00024-D.
- 8. J.A. Shaw and S. Kyriakides: *Acta Mater.*, 1997, vol. 45(2), pp. 683–700. https://doi.org/10.1016/S1359-6454(96)00189-9.
- S. Daly, G. Ravichandran, and K. Bhattacharya: *Acta Mater.*, 2007, vol. 55(10), pp. 3593–600. https://doi.org/10.1016/j.actamat. 2007.02.011.
- E.A. Pieczyska, S.P. Gadaj, W.K. Nowacki, and H. Tobushi: *Exp. Mech.*, 2006, vol. 46, pp. 531–42. https://doi.org/10.1007/s11340-006-8351-y.
- E.A. Pieczyska, H. Tobushi, and K. Kulasinski: Smart Mater. Struct., 2013, vol. 22(3), p. 035007. https://doi.org/10.1088/0964-1726/22/3/035007.
- 12. S. Tsimpoukis and S. Kyriakides: *Extreme Mech. Lett.*, 2024, vol. 73, 102263https://doi.org/10.1016/j.eml.2024.102263.
- K. Kazinakis, S. Kyriakides, and C.M. Landis: Extreme Mech. Lett., 2022, vol. 53, 101689https://doi.org/10.1016/j.eml.2022. 101689.
- C. Elibol and M.F.-X. Wagner: *Mater. Sci. Eng. A*, 2015, vol. 621, pp. 76–81. https://doi.org/10.1016/j.msea.2014.10.054.
- D. Delpueyo, A. Jury, X. Balandraud, and M. Grédiac: *Shape Mem. Superelasticity.*, 2021, vol. 7, pp. 462–90. https://doi.org/10.1007/s40830-021-00355-w.
- E. Bonnot, R. Romero, L. Mañosa, E. Vives, and A. Planes: *Phys. Rev. Lett.*, 2008, vol. 100, 125901https://doi.org/10.1103/PhysRevLett.100.125901.
- S. Qian, Y. Geng, Y. Wang, J. Ling, Y. Hwang, R. Radermacher, I. Takeuchi, and J. Cui: *Int. J. Refrig.*, 2016, vol. 64, pp. 1–19. h ttps://doi.org/10.1016/j.ijrefrig.2015.12.001.
- Y. Wu, E. Ertekin, and H. Sehitoglu: *Acta Mater.*, 2017, vol. 135, pp. 158–76. https://doi.org/10.1016/j.actamat.2017.06.012.
- L. Mañosa and A. Planes: Shape Mem. Superelasticity, 2024, vol. 10, pp. 1089–98. https://doi.org/10.1007/s40830-024-00477-x.
- A. Shen, D. Zhao, W. Sun, J. Liu, and C. Li: Scr. Mater., 2017, vol. 127, pp. 1–5. https://doi.org/10.1016/j.scriptamat.2016.08.030.
- F. Xiao, M. Jin, J. Liu, and X. Jin: Acta Mater., 2015, vol. 96, pp. 292–300. https://doi.org/10.1016/j.actamat.2015.05.054.
- G.J. Pataky, E. Ertekin, and H. Sehitoglu: *Acta Mater.*, 2015, vol. 96, pp. 420–7. https://doi.org/10.1016/j.actamat.2015.06.011.
- H.Y. Kim, Y. Ikehara, J.I. Kim, H. Hosoda, and S. Miyazaki: Acta Mater., 2006, vol. 54, pp. 2419–29. https://doi.org/10.1016/ i.actamat.2006.01.019.
- M. Tahara, H.Y. Kim, H. Hosoda, and S. Miyazaki: *Acta Mater.*, 2009, vol. 57(8), pp. 2461–9. https://doi.org/10.1016/j.actamat.20 09.01.037.
- S. Miyazaki: Shap. Mem. Superelasticity., 2017, vol. 3, pp. 279–314. https://doi.org/10.1007/s40830-017-0122-3.
- H.Y. Kim and S. Miyazaki: Shape Mem. Superelasticity., 2016, vol. 2, pp. 380–90. https://doi.org/10.1007/s40830-016-0087-7.
- L. Kong, B. Wang, S. Sun, Z. Gao, and X. Meng: *Mater. Lett.*, 2022, vol. 308, 131083https://doi.org/10.1016/j.matlet.2021. 131083.
- X. Zhu, M. Qian, X. Zhang, S. Zhong, Z. Jia, R. Zhang, A. Li, and L. Geng: *J. Alloys Compd.*, 2023, vol. 956, 170291https://doi.org/10.1016/j.jallcom.2023.170291.
- H. Xiang, Y. Guo, X. Zhao, Z. Li, B. Yang, N. Jia, H. Yan, and L. Zuo: Scr. Mater., 2024, vol. 244, 116002https://doi.org/10.1016/j.scriptamat.2024.116002.
- K.M. Golasiński, E.A. Pieczyska, M. Staszczak, M. Maj, T. Furuta, and S. Kuramoto: *Quant. InfraRed Thermogr. J.*, 2017, vol. 14, pp. 226–33. https://doi.org/10.1080/17686733.2017. 1284295.
- E.A. Pieczyska, M. Maj, K.M. Golasiński, M. Staszczak, T. Furuta, and S. Kuramoto: *Materials.*, 2018, vol. 11, p. 567. h ttps://doi.org/10.3390/ma11040567.
- 32. K.M. Golasiński, M. Staszczak, and E.A. Pieczyska: *Materials*, 2023, vol. 16, p. 3288. https://doi.org/10.3390/ma16093288.
- 33. K.M. Golasiński, M. Maj, L. Urbański, M. Staszczak, A. Gradys, and E.A. Pieczyska: *Quant. InfraRed Thermogr. J.*, 2023, vol. 21, pp. 259–76. https://doi.org/10.1080/17686733.2023.2205762.
- 34. T. Saito, T. Furuta, J.H. Hwang, S. Kuramoto, K. Nishino, N. Suzuki, R. Chen, A. Yamada, K. Ito, Y. Seno, T. Nonaka, H. Ikehata, N. Nagasako, C. Iwamoto, Y. Ikuhara, and T. Sakuma:

- Science, 2003, vol. 300, pp. 464-7. https://doi.org/10.1126/science. 1081957
- 35. M. Tahara, H.Y. Kim, T. Inamura, H. Hosoda, and S. Miyazaki: *J. Alloys Compd.*, 2013, vol. 577, pp. S404-7. https://doi.org/10.1016/j.jallcom.2011.12.113.
- M. Tahara, H.Y. Kim, T. Inamura, H. Hosoda, and S. Miyazaki: Acta Mater., 2011, vol. 59, pp. 6208–18. https://doi.org/10.1016/j.actamat.2011.06.015.
- 37. L.S. Wei, H.Y. Kim, and S. Miyazaki: *Acta Mater.*, 2015, vol. 100, pp. 313–22. https://doi.org/10.1016/j.actamat.2015.08.054.
- 38. M. Tahara, M.H.Y. Kim, H. Hosoda, and S. Miyazaki: Funct. Mater. Lett., 2009, vol. 2, pp. 79–82. https://doi.org/10.1142/S1793604709000600.
- 39. M. Tahara, H.Y. Kim, H. Hosoda, T. Nam, and S. Miyazaki: *Mater. Sci. Eng. A*, 2010, vol. 527, pp. 6844–52. https://doi.org/10.1016/j.msea.2010.07.052.
- K. Golasiński, M. Maj, W. Tasaki, E.A. Pieczyska, and H.Y. Kim: Metall. Mater. Trans. A., 2024, vol. 55, pp. 2509–18. https://doi. org/10.1007/s11661-024-07414-8.

- 41. S. Musiał, M. Nowak, and M. Maj: *Arch. Civ. Mech. Eng.*, 2019, vol. 19, pp. 1183–93. https://doi.org/10.1016/j.acme.2019.06.007.
- 42. K. Golasiński, E. Pieczyska, M. Maj, M. Staszczak, P. Świec, T. Furuta, and S. Kuramoto: *Archiv. Civ. Mech. Eng.*, 2020, https://doi.org/10.1007/s43452-020-00055-9.
- M. Nowak, M. Maj, S. Musiał, and T. Płociński: *Mater. Sci. Eng. A*, 2020, vol. 790, 139725https://doi.org/10.1016/j.msea.2020. 139725
- S. Musiał, M. Maj, L. Urbański, and M. Nowak: *Int. J. Solids Struct.*, 2022, vol. 238, pp. 111411-1–20. https://doi.org/10.1016/j.ijsolstr.2021.111411.
- 45. M. Nowak and M. Maj: *Archiv. Civ. Mech. Eng.*, 2018, vol. 18, pp. 630–44. https://doi.org/10.1016/j.acme.2017.10.005.
- M. Imran and X. Zhang: *Mater. Des.*, 2020, vol. 195, 109030h ttps://doi.org/10.1016/j.matdes.2020.109030.

Publisher's Note Springer Nature remains neutral with regard to jurisdictional claims in published maps and institutional affiliations.